(Received 16 September 2025, Accepted 26 November 2025, Scheduled 11 December 2025)

Multilayer Waveguide Bandpass Filters Based on Subwavelength CSRR and Omega Type Inclusions

Ivan E. Diaz[1, 2, *], Juan D. Baena[3], Carlos A. Suarez[1], and Hector F. Guarnizo[2]

[1] Department Engineering, Universidad Distrital F.J.C, Bogotá D.C., Colombia
[2] Department Engineering, Universidad El Bosque, Bogota D.C., Colombia
[3] Department of Physics, Universidad Nacional de Colombia, Bogotá D.C, Colombia

ABSTRACT: This paper presents the design, modeling, and experimental validation of multilayer waveguide bandpass filters employing two subwavelength resonator topologies: complementary split-ring resonators (CSRRs) and Ω-type cells. A hybrid methodology is adopted, combining equivalent circuit models, polarizability extraction from scattering parameters, and full-wave simulations. Mirror-symmetric configurations are introduced to suppress frequency splitting and improve band uniformity. For both CSRR and Ω arrays, equivalent LC parameters are derived and incorporated into a transmission-matrix framework, enabling accurate prediction of resonant behavior in cascaded layers. Numerical simulations in WR340 waveguides demonstrate that CSRR arrays achieve narrowband responses with high selectivity, while Ω-cells provide wider passbands and improved tolerance to interlayer spacing. Prototypes fabricated on high-purity aluminum sheets were measured using a vector network analyzer, confirming the theoretical and simulation results. The experimental data show close agreement with the proposed model, validating the scalability of the approach to multilayer designs. Quantitatively, the mirror-symmetric CSRR filter exhibits a center frequency of 2.49 GHz, a fractional bandwidth of 1.8%, and an insertion loss of 1.26 dB, whereas the Ω-based configuration achieves a 2.41 GHz center frequency, 5.6% fractional bandwidth, and 0.27 dB insertion loss. These results show that the Ω topology attains a wider fractional bandwidth and the consequently lower insertion loss predicted by fractional-bandwidth theory, rather than a reduction of intrinsic resonator loss. The proposed framework thus provides a systematic and efficient route for metamaterial filter synthesis, bridging analytical models, numerical simulations, and experimental validation.

1. INTRODUCTION

Since the introduction of Split Ring Resonators (SRR) by Pendry et al. [1], the design of subwavelength resonant structures has evolved towards compact and highly selective solutions for microwave applications. The complementary version, Complementary Split Ring Resonators (CSRR), proposed by Falcone et al. [2] and further developed for microstrip technology by Bonache et al. [3], has proven particularly effective in the implementation of miniaturized, high-Q bandpass filters. This concept builds upon earlier work on the modeling of resonant particles for metamaterials and filter design [4], as well as on the proposal of equivalent LC elements for compact filter designs [5]. These developments have established CSRRs as key functional building blocks in the realization of frequency selective surfaces and waveguide-based devices.

In parallel to CSRR-based designs, other subwavelength resonators have been proposed to enhance the control of electromagnetic wave propagation. Among them, Omega-shaped resonator stands out due to its intrinsic magnetoelectric coupling, enabling the simultaneous control of electric and magnetic responses. This property has been exploited to design components with improved rejection characteristics, dual-band operation, and sharper filter skirts. When being integrated into waveguide and planar technologies, Ω-type inclusions provide an additional degree of freedom in tailoring the dispersion and coupling characteristics of frequency-selective devices. Related approaches in planar technologies include the use of CSRR-loaded substrate integrated waveguides (SIWs) for miniaturized filter design [6]. Motivated by these capabilities, this work explores the combined use of CSRR and Ω-structures in bandpass filter design, aiming to achieve compact devices with high selectivity, low insertion loss, and enhanced control over transmission zeros.

Early implementations of CSRR-loaded waveguides already demonstrated their potential for compact bandpass filter design [7]. More recently, Aparicio et al. [8, 9] reported the design of evanescent-mode rectangular waveguide bandpass filters with transmission zeros using SRR inclusions, demonstrating improved selectivity and compactness through controlled coupling and resonant triplet configurations. Complementary approaches have also focused on improving the stopband and transmission-zero performance of CSRR-loaded filters through geometric asymmetry, as demonstrated by Bage and Das [10]. Aparicio et al. [8] later presented a methodology for designing rectangular waveguide bandpass filters with transmission zeros using high-Q CSRRs combined with irises. This approach achieves enhanced selectivity and compactness by exploiting the high-Q properties of CSRRs and carefully engineered coupling structures, setting a benchmark for state-of-the-art CSRR-based waveguide filter design.

* Corresponding author: Ivan Eduardo Diaz Pardo (iediaz@unbosque.edu.co).

In parallel, metasurface-based waveguide filters have emerged as a promising alternative for integrating subwavelength resonators into metallic waveguide platforms. The authors in [11] introduced a waveguide filter topology based on metasurfaces made of subwavelength slot resonators, demonstrating the feasibility of tailoring passband characteristics and beam control within a compact footprint. These developments highlight the versatility of CSRR and Omega-based metasurfaces in both planar and waveguide configurations, opening opportunities for advanced filter architectures.

While numerous studies have addressed the individual implementation of either CSRR or Ω-resonators, comparative analyses of both topologies within a common design methodology are still limited. In this work, each resonator type is employed in independent filter configurations, both designed under a unified hybrid modeling strategy that links equivalent circuit parameters with full-wave simulations. This approach enables the extraction of surface polarizabilities and their direct use in filter synthesis, providing accurate prediction of resonant behavior and coupling effects, as well as a straightforward pathway for iterative optimization without excessive computational cost. The proposed methodology is validated through the design and experimental characterization of mirror-symmetric waveguide bandpass filters, demonstrating how both CSRR- and Ω-based metasurfaces can achieve tailored frequency responses in compact and efficient devices.

The main objective of this work is to develop and validate a unified analytical-numerical methodology for the modeling and design of multilayer metamaterial filters integrated in waveguide technology. The proposed approach combines the surface-current formulation and transfer-matrix framework to describe the electromagnetic coupling between subwavelength resonant sheets. Two canonical topologies, complementary split ring resonator (CSRR) and Ω-shaped resonator, are analyzed to demonstrate the versatility of the method for bandwidth control and filter synthesis. The analytical predictions are validated through full-wave simulations and experimental measurements in WR340 waveguide configuration. Compared to previous works, this study provides (i) an explicit link between polarizability-based circuit parameters and measurable S-parameters, (ii) a parametric analysis of the dependence of the resonant frequency on the geometric parameters of the unit cell, and (iii) an experimental verification of the model under realistic loss conditions.

2. MODELING OF SUBWAVELENGTH WAVEGUIDE FILTERS

When a metamaterial is used as an electromagnetic filter, the polarizability of its constituent elements plays a decisive role in determining the frequencies that the filter can block, transmit, or reflect. Both electric and magnetic polarizabilities can be tailored to control the filter's frequency response, affecting the amplitude and phase of scattered fields. At resonance, high polarizability produces strong selective absorption, reflection, or transmission, while off-resonance behavior results in weak interaction with the incident wave, allowing other frequencies to pass almost unaltered.

From a filtering perspective, the real part of the polarizability governs phase shifts, while its imaginary part introduces attenuation and loss. This makes polarizability a key parameter not only for amplitude control but also for dispersion engineering in devices such as phase filters.

In practice, resonant inclusions such as split-ring resonators (SRRs), complementary SRRs (CSRRs), and Ω-shaped particles can be represented by an equivalent LC circuit, where the resonance frequency depends on the geometry and the surrounding dielectric environment. The inductance L accounts for the magnetic energy stored in the current loops, whereas the capacitance C represents the electric energy accumulated across the slots or gaps between metallic regions. Analytical models based on conformal mapping [12, 13] and later extended to thick resonators [14] express this dependence as

$$f_0 = \frac{1}{2\pi\sqrt{LC}}, \tag{1}$$

where f_0 denotes the fundamental resonance frequency of the metamaterial element. The geometrical parameters — ring width c, inter-ring spacing d, and outer radius r_{ext} — directly determine the values of L and C, and consequently shift f_0. This analytical relation enables predicting how fabrication tolerances or design variations affect the operating frequency without requiring extensive numerical optimization.

The equivalent parameters L and C of the CSRR can be derived from the quasi-static analysis of slotline structures using microstrip line theory combined with the Babinet duality principle [13, 15–17]. In this framework, the per-unit-length capacitance C_{pul} is obtained from the effective permittivity of the equivalent microstrip section, expressed through the complete elliptic integrals of the first kind $K(k)$ and $K'(k)$, where k and k_1 depend on the ring width c, separation d, and substrate thickness h. The total capacitance results from integrating the slot admittance along the ring circumference, yielding an expression that includes Struve and Bessel functions to capture fringing and substrate effects [18]. The inductance, on the other hand, is derived from the magnetic energy stored in the circulating currents around the apertures, giving:

$$L = \frac{\pi\mu_0 r_0}{8} F(k), \tag{2}$$

and

$$C = \frac{\pi^3\varepsilon_0}{2c^2}\int_0^\infty \frac{1}{k^2}\left[b_s\mathcal{B}(kb_s) - a_s\mathcal{B}(ka_s)\right]^2 \times \left[1 + \frac{1+\tanh(kh)\varepsilon_r}{1+\tanh(kh)/\varepsilon_r}\right] \mathrm{d}k. \tag{3}$$

where $F(k) = K(k)/K'(k)$, $a_s = r_0 - c/2$, $b_s = r_0 + c/2$, and $\mathcal{B}(x) = S_0(x)J_1(x) - S_1(x)J_0(x)$, with S_n and J_n denoting the Struve and Bessel functions of order n, respectively. These parameters depend directly on the geometric dimensions and substrate properties, providing a physical link between the unit-cell geometry and the resonance condition given by Eq. (1). The

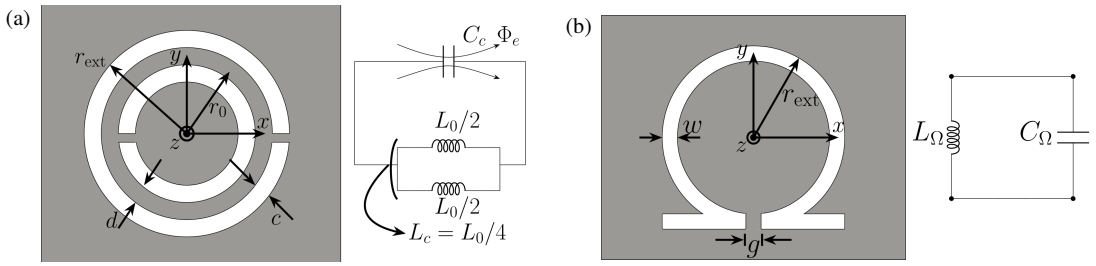

FIGURE 1. Subwavelength resonant inclusions and their equivalent circuits. (a) Complementary split-ring resonator (CSRR) unit cell, where L_{CSRR} and C_{CSRR} represent the inductive and capacitive coupling between the concentric apertures. (b) Ω-shaped inclusion, whose external radius r_{ext} defines the magnetic inductance L_Ω, while the lower gap provides the capacitive coupling C_Ω. In both cases, the gray regions correspond to metallic areas and the white regions to etched apertures. Both topologies exhibit equivalent LC resonant behavior and can be modeled within the same analytical framework.

same analytical framework extends naturally to the Ω-type inclusion, which exhibits an analogous LC behavior under transverse electric excitation. Figure 1 illustrates both resonator geometries and their equivalent circuit representations.

As expressed in Eq. (3), the metallic thickness h influences the coupling capacitance through the factor $(1 + \tanh(kh)\epsilon_r)/(1 + \tanh(kh)/\epsilon_r)$, which accounts for the confinement of fringing electric fields in the slot region. Variations in h slightly modify C_c and, consequently, the resonance frequency f_0 in Eq. (1). In this work, h was fixed to 1 mm, a value sufficiently small to preserve the validity of the Babinet principle and to ensure that thickness-related dispersion effects remain negligible in accordance with Pulido-Mancera et al. (2013).

Finally, substituting the calculated values of L and C into (1) yields the resonance frequency f_0, explicitly relating the geometry and substrate parameters to the electromagnetic response of the resonant cell. Table 1 summarizes the calculated inductance, capacitance, and resulting f_0 values for different outer radii r_{ext}, demonstrating that small geometric variations lead to predictable shifts in the resonance frequency. This confirms that the analytical model inherently captures the sensitivity of the resonant response to dimensional tolerances without the need for iterative full-wave optimization.

TABLE 1. Calculated inductance L, capacitance C, and resonance frequency f_0 for a CSRR as a function of the outer radius r_{ext}, obtained from the analytical model (1).

r_{ext} [mm]	L [nH]	C [pF]	f_0 [GHz]	$\Delta f_0/f_0$ [%]
8.82	5.78	0.83	2.28	+2.88
8.91	5.86	0.85	2.25	+1.42
9.00	5.93	0.86	2.21	0
9.09	6.00	0.88	2.18	−1.39
9.18	6.08	0.89	2.15	−2.74

A parametric full-wave analysis was carried out to verify the sensitivity of the resonant frequency to dimensional variations predicted by the analytical model. The outer radius r_{ext} was varied while keeping h, l, and the remaining geometrical parameters constant. The simulated S_{11} responses exhibit a monotonic frequency shift of f_0, in full agreement with the proportional dependence established by Eq. (1). This confirms that the analytical formulation inherently captures the geometric sensitivity of the resonance without requiring iterative full-wave optimization. The influence of the metallic thickness h on the capacitance term, already demonstrated in previous works ([13, 19]), was kept constant at $h = 1$ mm in this study to ensure the thin-sheet regime and preserve the validity of the Babinet principle for both CSRR and Ω configurations.

2.1. Surface Electric and Magnetic Current Theory

The electromagnetic response of a metasurface can be modeled in terms of induced surface currents, which arise when an incident wave interacts with its periodic resonant inclusions. Depending on the nature of the inclusion, the dominant interaction can be associated with electric surface currents $\mathbf{J}_s$ or magnetic surface currents $\mathbf{K}_s$. These currents represent equivalent distributed sources that reproduce the scattering produced by the physical structure.

The interaction of a plane wave with the metasurface can be described in terms of incident and reflected fields on each side of the structure. Figure 2 illustrates the adopted convention: on the left side, $\mathbf{E}_1^+$ and $\mathbf{H}_1^+$ denote the incident fields, while $\mathbf{E}_1^-$ and $\mathbf{H}_1^-$ correspond to the reflected fields. On the right side, only the transmitted field components $\mathbf{E}_2^-$ and $\mathbf{H}_2^-$ are depicted, since the analysis considers a wave propagating from left to right. Due to the symmetry of the structure, the opposite case (right-to-left propagation) can be obtained by analogy. This field decomposition provides the basis for defining the surface electric and magnetic currents, $\mathbf{J}_s$ and $\mathbf{K}_s$, employed in the theoretical formulation.

From a microscopic point of view, each resonator can be modeled as an induced dipole (electric or magnetic) whose strength is proportional to the local field and whose proportionality factor is the polarizability (α_e or α_m). The presence of nearby dipoles modifies the local field through mutual coupling, quantified by a feedback coefficient C, leading to an effective polarizability:

$$\hat{\alpha}_e = \frac{\alpha_e}{1 - C\alpha_e}, \quad \hat{\alpha}_m = \frac{\alpha_m}{1 - C\alpha_m}. \tag{4}$$

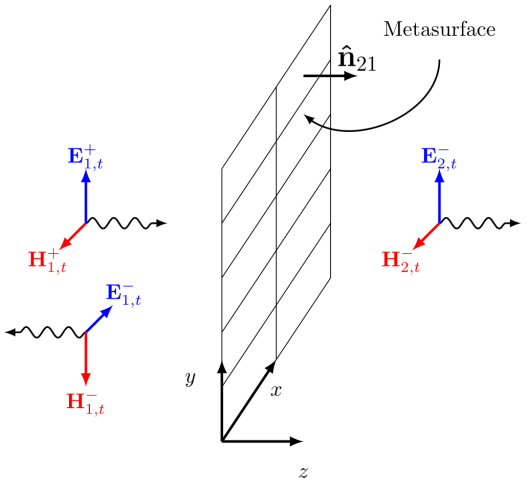

FIGURE 2. Plane-wave decomposition at the metasurface interface showing incident ($\mathbf{E}_1^+, \mathbf{H}_1^+$) and reflected ($\mathbf{E}_1^-, \mathbf{H}_1^-$) fields on the left, and transmitted fields ($\mathbf{E}_2^-, \mathbf{H}_2^-$) on the right. The surface electric current $\mathbf{J}_s$ and magnetic current $\mathbf{K}_s$ represent the induced response of the metasurface. The sign convention for ($\pm$) follows the formulation used in [20], where the superscript indicates the propagation direction with respect to the interface normal.

This effective polarizability incorporates both the intrinsic dipole response and the collective effect of the array, which is particularly relevant in subwavelength periodic arrangements where coupling is strong [20–22].

2.1.1. Electric Surface Currents

For electrically resonant inclusions, the electric dipole moment is expressed as:

$$\mathbf{p} = \epsilon_0 \hat{\alpha}_e \mathbf{E}_1^+. \tag{5}$$

As illustrated in Figure 2, the discontinuity of the tangential magnetic field across the metasurface defines the induced electric surface current density. Following the formulation in [20], it can be expressed as:

$$\mathbf{J}_s = \hat{\mathbf{n}}_{21} \times (\mathbf{H_2} - \mathbf{H_1}) = \hat{\mathbf{n}}_{21} \times \left(\mathbf{H}_2^- - \mathbf{H}_1^+ - \mathbf{H}_1^-\right), \tag{6}$$

$$\mathbf{J}_s = \sqrt{\frac{\epsilon_0}{\mu_0}} \left(-\mathbf{E}_2^- + \mathbf{E}_1^+ - \mathbf{E}_1^-\right), \tag{7}$$

where $\hat{\mathbf{n}}_{12}$ is the unit normal vector directed from region 1 to region 2, and $\mathbf{H}_1$ and $\mathbf{H}_2$ denote the total magnetic fields immediately on each side of the interface. This boundary condition establishes the physical basis linking the macroscopic electromagnetic fields with the equivalent circuit representation of the metasurface.

By expressing the total magnetic fields in terms of the incident and reflected plane-wave components, Eq. (6) leads to the equivalent form:

$$\mathbf{J}_s = j\omega \mathbf{P}_s = j\omega\epsilon_0 \frac{\hat{\alpha}_e}{a^2} \mathbf{E}_1^+ = \sqrt{\frac{\epsilon_0}{\mu_0}} \left(-\mathbf{E}_2^- + \mathbf{E}_1^+ - \mathbf{E}_1^-\right), \tag{8}$$

where a^2 denotes the area of the unit cell. This normalization ensures that the extracted polarizability represents the average response per unit surface area, consistent with the homogenization approach of metasurfaces.

From this relation, the electric polarizability can be directly obtained from the S-parameters as:

$$\hat{\alpha}_e = j\frac{a^2}{k_0}\left(S_{21} + S_{11} - 1\right). \tag{9}$$

2.1.2. Magnetic Surface Currents

For magnetically resonant inclusions, the magnetic dipole moment is given by

$$\mathbf{m} = \hat{\alpha}_m \mathbf{H}_1^+. \tag{10}$$

In analogy with the electric case, the discontinuity of the tangential electric field across the metasurface defines the induced magnetic surface current density. According to the boundary condition formulation described in [20], it can be written as:

$$\mathbf{K}_s = -\hat{\mathbf{n}}_{12} \times (\mathbf{E}_2 - \mathbf{E}_1), \tag{11}$$

where $\hat{\mathbf{n}}_{12}$ is the unit normal vector directed from region 1 to region 2, and $\mathbf{E}_1$ and $\mathbf{E}_2$ are the total electric fields at each side of the interface. This relation establishes the dual boundary condition associated with the magnetic response of the metasurface.

By expressing the total fields in terms of the forward and backward plane-wave components (see Figure 2), Eq. (11) becomes:

$$\mathbf{K}_s = j\omega\mu_0 \frac{\hat{\alpha}_m}{a^2} \mathbf{H}_1^+ = -\hat{\mathbf{n}}_{12} \times \left(\mathbf{E}_2^- - \mathbf{E}_1^+ - \mathbf{E}_1^-\right). \tag{12}$$

The term $\mathbf{H}_1^+$ in Eq. (12) is directly related to the incident electric field through the transverse field relation $\mathbf{H}_1^+ = 1/\eta_0 \hat{\mathbf{n}}_{12} \times \mathbf{E}_1^+$, where $\eta_0 = \sqrt{\mu_0/\epsilon_0}$ is the intrinsic impedance of free space. Substituting this expression into Eq. (12) yields the equivalent representation in terms of the electric field components, consistent with the wave decomposition shown in Figure 2. This step establishes the electromagnetic duality between the electric and magnetic surface responses, allowing both $\hat{\alpha}_e$ and $\hat{\alpha}_m$ to be expressed as functions of the measurable S-parameters.

The magnetic polarizability in terms of the S-parameters is then obtained as:

$$\hat{\alpha}_m = j\frac{a^2}{k_0}\left(S_{21} - S_{11} - 1\right). \tag{13}$$

This formulation underscores the physical link between the induced dipole moments and measurable scattering parameters, bridging microscopic electromagnetic interactions with macroscopic filter behavior. By applying these relations, both electric and magnetic polarizabilities can be extracted directly from simulation or measurement data, enabling the construction of accurate equivalent circuit models and the comparative analysis of different resonator topologies (such as CSRR and Ω inclusions) under a unified parameter framework.

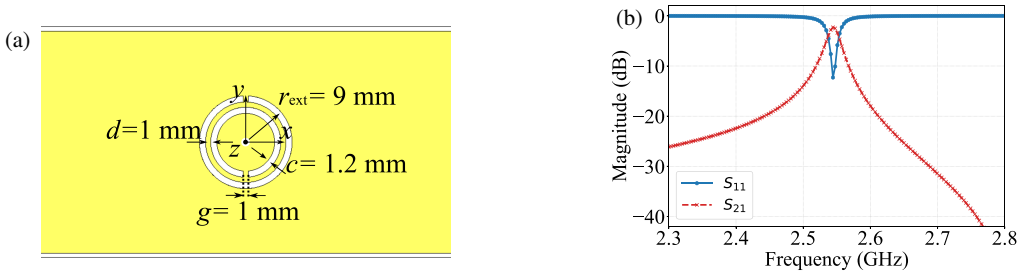

FIGURE 3. CSRR model with a metallic sheet thickness of $h = 1$ mm. (a) Cell dimensions. (b) Simulated S-parameters.

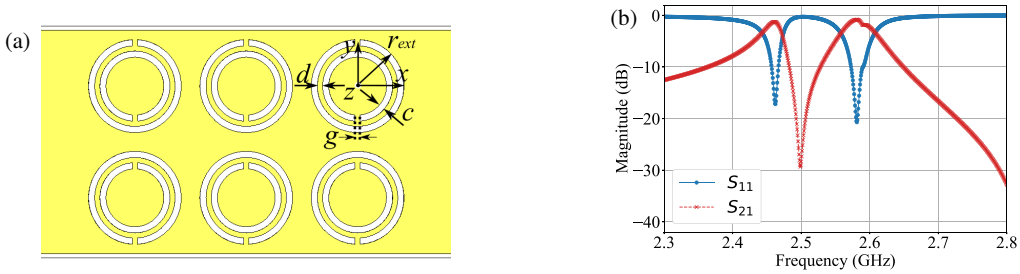

FIGURE 4. Configuration of a six-cell CSRR array in the waveguide cross section. (a) Array without mirror-symmetry. (b) Simulated scattering parameters S_{11} and S_{21}.

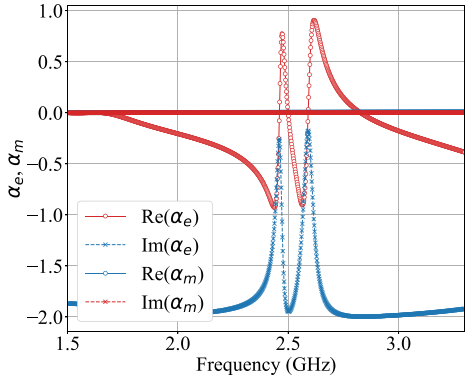

FIGURE 5. Extracted electric and magnetic polarizabilities of the six-cell CSRR array, showing both real and imaginary components around the resonance.

2.2. Waveguide Filter Model for a Single Layer

Previous studies on waveguide filters based on CSRR-type metamaterials have demonstrated highly selective passband behavior [23]. In this work, we propose integrating a set of uniformly distributed CSRR cells into a single metallic plate, leveraging their electrically small size to preserve the passband response while avoiding significant additional losses.

Figure 3 presents the first simulation of a CSRR etched on an aluminum sheet, considering the material's conductive losses and a plate thickness of $h = 1$ mm. The resulting scattering parameters (S-parameters) reveal the resonance behavior of the structure, where the transmission (S_{21}) and reflection (S_{11}) responses clearly exhibit its frequency-selective characteristics.

Because CSRRs are subwavelength resonators, multiple units can be arranged within the cross-section of a single-mode waveguide, allowing optimization of both bandwidth and peak transmission at the resonant frequency. Compared with conventional cavity resonators, these implementations are more compact and flexible.

For an array of six cells without mirror-symmetry (See Figure 4), the surface current distribution induces a frequency splitting effect, clearly visible in both the S-parameters and in the electric polarizability α_e.

The electromagnetic characterization of CSRR arrays is not limited to the inspection of S-parameters. A deeper understanding of their behavior requires analyzing the response in terms of surface electric and magnetic polarizabilities. In this sense, the surface current density formalism (presented in the previous section) enables the direct extraction of $\hat{\alpha}_E$ and $\hat{\alpha}_m$ from the S-parameters, establishing an explicit link between full-wave simulation results and equivalent circuit models.

For electrically resonant inclusions, the electric surface current density $\mathbf{J}_s$ is related to the electric polarizability (Eqs. (8) and (9)), while for magnetically resonant inclusions, the magnetic surface current density $\mathbf{K}_s$ is associated with the magnetic polarizability (Eqs. (12) and (13)). Figure 5 illustrates the behavior of α_e and α_m, showing that these structures exhibit a stronger electric polarizability at the global resonance frequency of the array. In addition, a double polarizability response is observed, related to the frequency splitting shown in Figure 4.

To suppress this splitting effect, a horizontal mirror-symmetry plane is introduced at the midpoint of the metallic sheet. This modification changes the current distribution between the upper and lower arrays. The new configuration is presented in Figure 6.

In this case, the polarizability is dominated by a single maximum around the resonant frequency, while the magnetic polarizability remains negligible across the entire frequency range. This occurs because the CSRR geometry generates a current

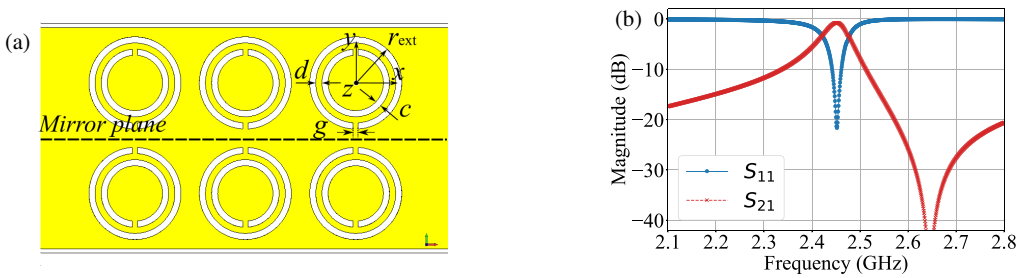

FIGURE 6. Six-cell CSRR array under mirror-symmetric configuration. (a) Geometrical layout. (b) Simulated scattering parameters S_{11} and S_{21}.

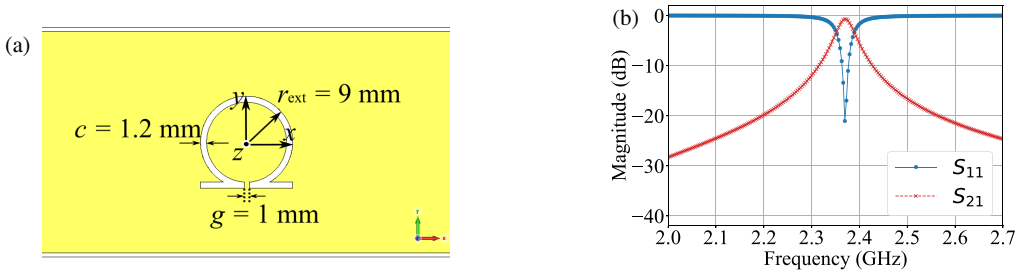

FIGURE 7. Ω-cell implemented on a metallic sheet with thickness $h = 1$ mm. (a) Geometry of the unit cell. (b) Scattering parameters S_{11} and S_{21}.

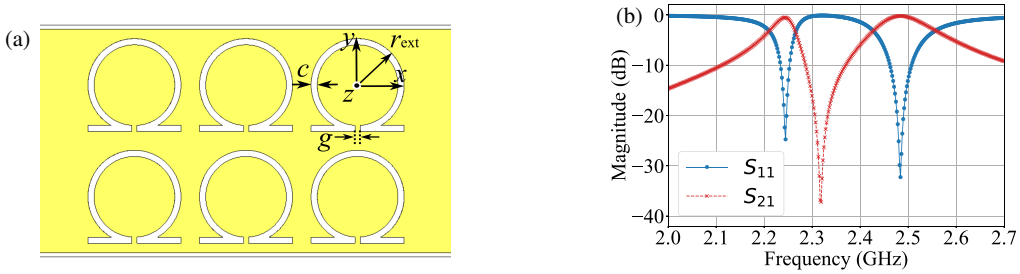

FIGURE 8. Array of Ω resonators implemented on a metallic sheet. (a) Uniform layout of the unit cells. (b) Simulated Scattering parameters S_{11} and S_{21}.

distribution that weakly couples to magnetic fields. By adjusting the size or shape of the slots, the balance between electric and magnetic polarizability can be tuned. Moreover, in CSRR arrays, interactions between neighboring cells can also affect the effective polarizability of the system. However, in the proposed mirror-symmetric configuration, such interactions suppress frequency splitting.

As an additional proposal, the Omega-shaped cell is introduced, named after its resemblance to the Greek letter Ω. This geometry behaves as a resonator over a broader frequency range compared with the CSRR. Its geometry and resonant response are shown in Figure 7.

The Ω-cell also acts as a subwavelength resonator with metamaterial properties, responding primarily to the incident electric field and inducing a strong electric polarizability at its resonant frequency. Compared with the CSRR, it provides a wider bandwidth and improved performance when arranged in a transverse metallic sheet. Because of its subwavelength nature, multiple Ω-cells can be grouped within a compact area. Figure 8 shows an array of six uniformly distributed Ω-cells on a metallic plate.

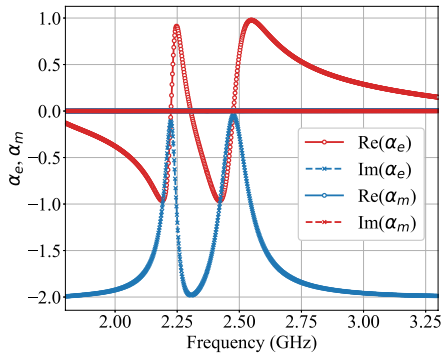

FIGURE 9. Real and imaginary parts of the extracted electric (α_e) and magnetic (α_m) polarizabilities for the Ω-cell array.

Figure 8(b) presents the scattering parameters of this configuration, where two clearly defined resonant bands appear. This splitting directly impacts the constitutive parameters of the structure, as evidenced by significant variations in magnetic polarizability (see Figure 9). Such variations confirm the strongly dispersive and anisotropic nature of Omega-type inclusions, suggesting their potential for selective filtering and phase-control applications.

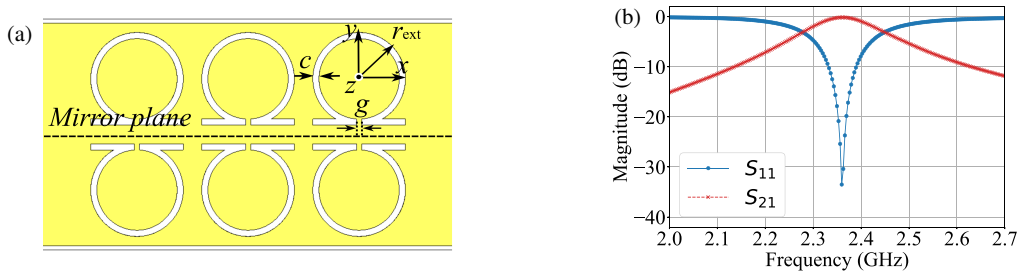

FIGURE 10. Mirror-symmetric configuration of a six-cell Ω array. (a) Unit-cell distribution showing the horizontal symmetry plane. (b) Simulated scattering parameters S_{11} and S_{21}, illustrating the passband broadening and improved transmission uniformity due to the symmetric field distribution.

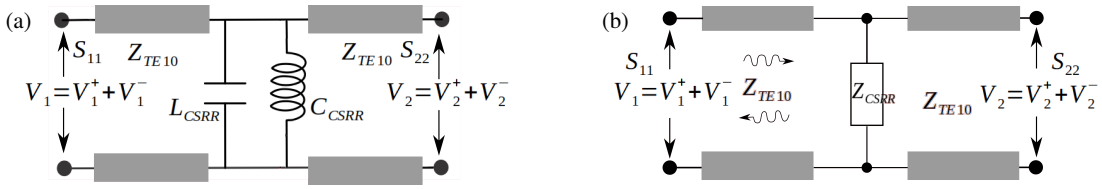

FIGURE 11. Equivalent circuit model for a single CSRR array layer: (a) Circuital representation with L and C. (b) Equivalent impedance representation.

Similar to the CSRR case, mirror-symmetry is proposed to achieve a uniform current distribution between the upper and lower parts of the array and thus eliminate frequency splitting.

Incorporating mirror-symmetry in Ω-cell arrays not only suppresses frequency splitting but also modifies the balance between polarizabilities. With symmetry enforced, the electric polarizability α_e remains dominant. This condition is ideal for bandpass filter design, as it allows closer spacing between cells without introducing undesired magnetic couplings. As a result, the structure becomes more compact and produces a well-defined transmission band. The passband widening observed in this configuration is primarily attributed to the modified current distribution that enhances coupling between adjacent cells. Although a small capacitive interaction exists between the parallel metallic traces of the two rows, its contribution to the bandwidth is secondary compared with the dominant effect of the symmetric field distribution, which effectively reduces frequency splitting and improves transmission uniformity. Figure 10 illustrates the mirror-symmetric configuration and its simulated scattering parameters, highlighting the broadened passband obtained under symmetric excitation. Compact wideband responses of similar nature have also been reported using complementary-loaded SRRs (CL-SRRs) in waveguide configurations, further confirming the versatility of resonator-based approaches for broadband filter synthesis [24].

2.3. Equivalent Circuit Model

CSRR and Ω cell arrays exhibit the characteristic behavior of bandpass filters. One approach to broaden the bandwidth of these devices is by implementing multiple metallic sheets arranged in cascade along the propagation direction. These sheets will be referred to as layers, and each of them can be modeled as an equivalent RLC circuit, where resistance is negligible ($R = 0$).

In the literature, circuit modeling of metamaterial cells has been addressed through their effective electromagnetic properties (permittivity, permeability, and polarizability), using passive circuit representations composed of inductances (L), capacitances (C), and, in some cases, resistances (R) to account for losses [1]. This approach enables the construction of analytical models that capture the resonant behavior of the structure in electrical terms, facilitating the interpretation of phenomena such as resonance, dispersion, and absorption through circuit elements.

In particular, it has been demonstrated that there is a formal equivalence between polarizability-based models and circuit models, especially for waveguide-fed structures [25]. This equivalence validates the use of circuit models to represent electromagnetic coupling between layers and allows explicit relationships to be established between circuit parameters and properties extracted from simulations or measurements. To determine the values of L and C in each layer, the characterization of the scattering parameters S_{11} and S_{21} obtained from numerical simulations of each sheet is employed. Figure 11 illustrates the equivalent circuit model for a single layer, based on a representation of its surface impedance, which is directly related to the induced electric and magnetic currents [26]. The inductance and capacitance values can be calculated using Eqs. (16) and (17), derived from the spectral behavior of the system. The resonant behavior of a CSRR or Ω cell then follows the classical LC relation given in Eq. (1), where f_0 is obtained from the extracted L and C for each topology.

To obtain the effective inductance and capacitance values, the characteristic impedance of the waveguide in the dominant TE_{10} mode is taken as a starting point, given by:

$$Z_{\mathrm{TE}_{10}} = \frac{\eta_0}{\sqrt{1 - \left(\frac{f_c}{f}\right)^2}}, \tag{14}$$

where η_0 is the wave impedance in free space, and f_c is the cutoff frequency of the waveguide in mode (m, n) [27, 28]. The equivalent circuit can also be characterized by its quality factor Q_L, which is related to the 3-dB bandwidth BW and the center (resonant) frequency f_0 of the passband as:

$$Q_L = \frac{f_0}{\mathrm{BW}_{3\,\mathrm{dB}}}. \tag{15}$$

Here, f_0 denotes the resonant (center) frequency corresponding to the peak transmission of the filter, and Q_L represents the loaded quality factor, obtained directly from the simulated or measured S-parameter responses [23]. This definition inherently accounts for both the intrinsic losses of the resonant cells and the external coupling between layers and ports, thereby characterizing the overall performance of the multilayer filter. In this work, Q_L is employed as an *effective parameter* to determine the equivalent inductance and capacitance of each resonant sheet, providing an accurate estimation of the bandwidth and coupling effects without explicitly introducing a loss resistance. Since the objective is to predict the passband behavior of single- and multilayer configurations rather than to extract intrinsic dissipation, the unloaded quality factor Q_0 is not explicitly used in the circuit model.

Knowing Q_L and $Z_{\mathrm{TE}_{10}}$, the capacitance C and inductance L of the cell model can be calculated as:

$$C = \frac{Q_L}{2\pi f_0 Z_{\mathrm{TE}_{10}}}, \tag{16}$$

$$L = \frac{Z_{\mathrm{TE}_{10}}}{2\pi f_0 Q_L}. \tag{17}$$

2.4. Scattering and Transfer-Matrix Framework for Multilayer Modeling

In the previous sections, the electromagnetic formulation was expressed in terms of tangential field components (E_t, H_t) to describe the induced surface currents and polarizabilities. For the network representation, it is more convenient to employ the power-wave formalism, in which the incident and reflected quantities are normalized with respect to the wave impedance of the dominant mode ($Z_{\mathrm{TE}_{10}}$) [27]. Accordingly, the quantities V^+ and V^- used in the scattering-matrix formulation represent voltage amplitudes proportional to the normalized power waves,

$$a_i = \frac{V_i^+}{\sqrt{Z_{\mathrm{TE}_{10}}}}, \quad b_i = \frac{V_i^-}{\sqrt{Z_{\mathrm{TE}_{10}}}}. \tag{18}$$

This convention ensures energy consistency between the field-based formulation and the circuit-based model, allowing the direct transformation between $[S]$- and $[T]$-parameters under the same physical normalization.

Based on the equivalent circuit representation shown in Figure 11, the response of the system can be conveniently described using the scattering matrix formalism. In this representation, the incident and reflected wave amplitudes at each port are expressed in terms of power-normalized quantities, which are proportional to the voltage waves normalized by the characteristic impedance of the dominant mode $Z_{\mathrm{TE}_{10}}$ [28]. The general two-port relation between these amplitudes is given by:

$$\begin{bmatrix} V_1^- \\ V_2^- \end{bmatrix} = \begin{bmatrix} S_{11} & S_{12} \\ S_{21} & S_{22} \end{bmatrix} \begin{bmatrix} V_1^+ \\ V_2^+ \end{bmatrix}, \tag{19}$$

where V_i^+ and V_i^- represent the forward (incident) and backward (reflected) voltage waves at port i, respectively. This formulation provides a direct link between the electromagnetic model of the metasurface and its equivalent two-port network representation, facilitating the subsequent derivation of the transfer matrix $[T]$ for multilayer configurations [27].

For metasurface-type structures, under linear conditions and in the absence of nonreciprocal materials, the reciprocity criterion holds, implying a symmetric scattering matrix. In this framework, each port is characterized by its forward and backward power-normalized waves, and for a two-port network the S-parameters are defined as:

$$S_{11} = \left.\frac{V_1^-}{V_1^+}\right|_{V_2^+=0}, \quad S_{21} = \left.\frac{V_2^-}{V_1^+}\right|_{V_2^+=0}, \tag{20}$$

$$S_{22} = \left.\frac{V_2^-}{V_2^+}\right|_{V_1^+=0}, \quad S_{12} = \left.\frac{V_1^-}{V_2^+}\right|_{V_1^+=0}. \tag{21}$$

This representation is fundamental for multilayer analysis, as it enables cascading of subsystems. Subsequently, the scattering matrix can be converted into a transfer matrix T, which facilitates the analysis of forward/backward propagation. For a single transverse sheet represented by an equivalent shunt impedance Z_{CSRR} (the effective sheet impedance), we start from:

$$V_1 = V_1^+ + V_1^-, \quad I_1 = \frac{V_1^+ - V_1^-}{Z_0}. \tag{22}$$

The voltage-current relation across the shunt sheet is:

$$V_1 = I_1 \frac{Z_{\mathrm{CSRR}} Z_0}{Z_{\mathrm{CSRR}} + Z_0}. \tag{23}$$

which yields

$$V_1^+ + V_1^- = \left(\frac{Z_{\mathrm{CSRR}}}{Z_{\mathrm{CSRR}} + Z_0}\right)\left(V_1^+ - V_1^-\right). \tag{24}$$

Hence,

$$S_{11} = \frac{V_1^-}{V_1^+} = \frac{-Z_0}{2Z_{\mathrm{CSRR}} + Z_0}. \tag{25}$$

For S_{21}, with excitation at port 1 and $V_2^+ = 0$:

$$I_2^- = \frac{Z_{\mathrm{CSRR}}}{Z_{\mathrm{CSRR}} + Z_0} I_1, \quad I_2^- = \frac{V_2^-}{Z_0}, \tag{26}$$

so that

$$\frac{V_2^-}{Z_0} = \frac{Z_{\mathrm{CSRR}}}{Z_{\mathrm{CSRR}} + Z_0} \frac{V_1^+ - V_1^-}{Z_0}, \tag{27}$$

and

$$V_2^- = \frac{Z_{\text{CSRR}}}{Z_{\text{CSRR}} + Z_0} V_1^+ (1 - S_{11}). \tag{28}$$

Therefore,

$$S_{21} = \frac{V_2^-}{V_1^+} = \frac{Z_{\text{CSRR}}}{Z_{\text{CSRR}} + Z_0}(1 - S_{11}). \tag{29}$$

Collecting the above, the S-matrix for a symmetric shunt impedance model reads:

$$\begin{bmatrix} V_1^- \\ V_2^- \end{bmatrix} = \begin{bmatrix} \frac{-Z_0}{2Z_{\text{CSRR}}+Z_0} & \frac{Z_{\text{CSRR}}}{Z_{\text{CSRR}}+Z_0}(1 - S_{11}) \\ \frac{Z_{\text{CSRR}}}{Z_{\text{CSRR}}+Z_0}(1 - S_{11}) & \frac{-Z_0}{2Z_{\text{CSRR}}+Z_0} \end{bmatrix} \begin{bmatrix} V_1^+ \\ V_2^+ \end{bmatrix}. \tag{30}$$

To enhance the filter response, a second metallic sheet (a second CSRR array) can be cascaded, as shown in Figure 12.

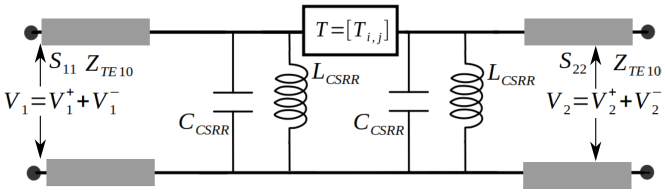

FIGURE 12. Circuit model for two cascaded CSRR-array sheets. The waveguide section between sheets is represented by a transmission matrix $[T]$.

The transfer (or chain) matrix $[T]$ describes the propagation of power waves through a two-port network. Using the power-wave definition, one has:

$$\begin{bmatrix} a_1 \\ b_1 \end{bmatrix} = \begin{bmatrix} T_{11} & T_{12} \\ T_{21} & T_{22} \end{bmatrix} \begin{bmatrix} b_2 \\ a_2 \end{bmatrix}. \tag{31}$$

In terms of the scattering matrix $[S]$, the transfer matrix can be written as:

$$\begin{bmatrix} a_1 \\ b_1 \end{bmatrix} = \frac{1}{S_{21}} \begin{bmatrix} 1 & -S_{22} \\ S_{11} & S_{12}S_{21} - S_{11}S_{22} \end{bmatrix} \begin{bmatrix} b_2 \\ a_2 \end{bmatrix}. \tag{32}$$

For two metamaterial sheets separated by a waveguide segment, the propagation in that segment must be characterized. Unlike transmission lines, where distributed parameters R, L, G, and C describe signal propagation, in waveguides a modal description is required. The inter-sheet segment is therefore modeled by its transfer matrix T_g, representing the propagation of the dominant TE_{10} mode over a length l. Along the longitudinal coordinate z, the field can be written as a superposition of forward and backward waves:

$$E(z) = E^+ e^{-\gamma z} + E^- e^{\gamma z}, \tag{33}$$

where $\gamma = \alpha + j\beta$ is the complex propagation constant (with α the attenuation constant and β the phase constant). For a segment of length l, defining the input plane at $z = 0$ and the output plane at $z = l$:

$$E(0) = E_1^+ + E_1^-, \quad E(l) = E_2^+ e^{-\gamma l} + E_2^- e^{\gamma l}. \tag{34}$$

In transfer-matrix form:

$$\begin{bmatrix} E_1^+ \\ E_1^- \end{bmatrix} = \underbrace{\begin{bmatrix} e^{-\gamma l} & 0 \\ 0 & e^{\gamma l} \end{bmatrix}}_{T_g} \begin{bmatrix} E_2^+ \\ E_2^- \end{bmatrix}. \tag{35}$$

In the lossless case ($\alpha = 0$), the propagation matrix T_g is reduced to a pure phase delay. The overall cascaded system (comprising the metasurface sheet, the intermediate waveguide section, and the second sheet) can therefore be expressed as:

$$T_{\text{total}} = T_1 \cdot T_g \cdot T_2, \tag{36}$$

where T_1 and T_2 are the transfer matrices of the individual sheets (CSRR or Ω), previously modeled through their equivalent resonant cells. The transformation between the scattering and transfer matrices follows the standard formulation described in [28, 29], ensuring consistency between the electromagnetic and circuit representations of the multilayer system.

Figure 13 shows the increase in the passband bandwidth when two CSRR-based metamaterial layers are cascaded. This behavior is consistent with coupled-resonator theory, where the overall response results from the combined effect of each cell. A key constraint to preserve the intended operation is the length of the interposed waveguide section, which here is set to the minimum feasible distance ($l = 50\,\text{mm}$) to avoid direct electromagnetic coupling between metallic sheets. For both CSRR- and Ω-based filters, this distance corresponds to approximately half the guided wavelength at their respective resonance frequencies ($l \approx 0.48, \lambda_g$), ensuring that the intermediate guide section behaves as a phase inverter and minimizes evanescent coupling between layers. Maintaining the same spacing for both configurations allows a consistent comparison while guaranteeing weak interlayer interaction. Similar design considerations have been reported in the synthesis of cascaded singlets for waveguide filters, where the inter-resonator separation is adjusted to achieve the desired phase relation and compensate for mismatch between analytical and physical implementations [8]. In Figure 13(b), the equivalent two-layer model is shown, where the intermediate guide segment is represented by T_g.

Extending the analysis to two Ω-cell layers yields a similar trend to the CSRR structures, with an increase in bandwidth and a broader passband transmission. Cascading the sheets with a minimal separation to avoid parasitic coupling preserves the resonant response without introducing extra modes. Figure 14 shows the scattering parameters for the two-layer configuration, demonstrating an expanded transmission range compared with a single sheet. This confirms that Ω-cells, with dominant electric polarizability and a broader frequency response, are well suited for wide-coverage bandpass filter designs in multilayer structures.

3. SIMULATION RESULTS FOR MULTILAYER CONFIGURATIONS

The theoretical framework presented in Section 2 establishes the analytical and network foundations required to predict the

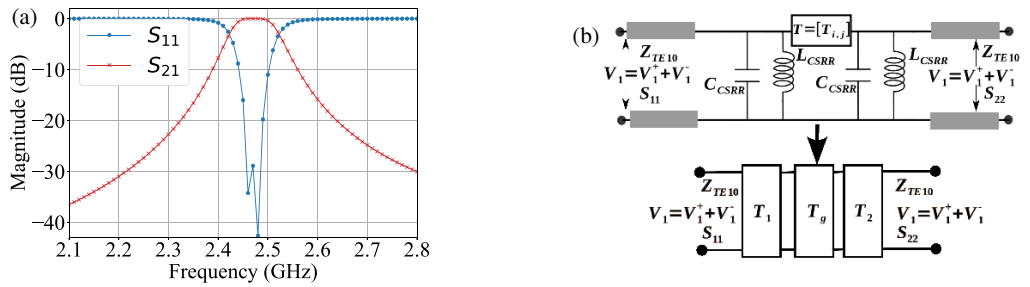

FIGURE 13. Model of the two-layer CSRR metamaterial filter. (a) Transformation of the overall transfer matrix T_{total} into S-parameters. (b) Equivalent circuit representation, where the interlayer section is described by T_g of length $l = 50\,\text{mm}$.

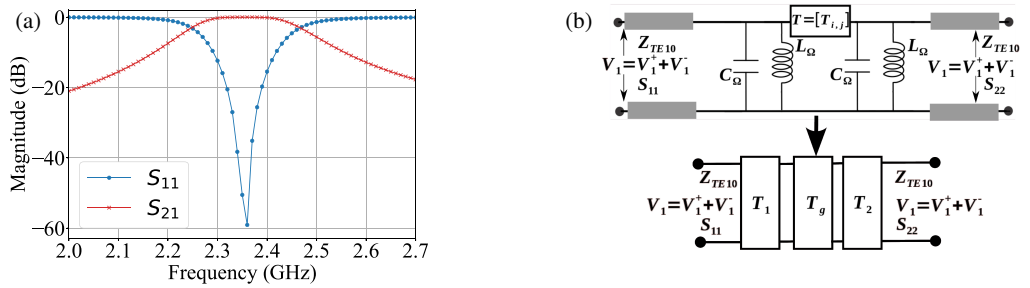

FIGURE 14. Model of the two-layer Ω metamaterial filter. (a) Transformation of the overall transfer matrix T_{total} into S-parameters. (b) Equivalent circuit representation, where the interlayer section is described by T_g of length $l = 50\,\text{mm}$.

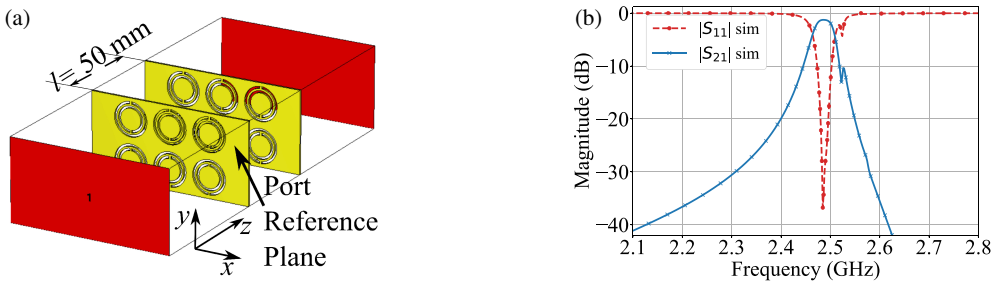

FIGURE 15. Simulation of a two-layer CSRR-based filter. (a) Three-dimensional model within a WR340 waveguide with an intelayer spacing l. (b) Simulated scattering parameters S_{11} and S_{21}. The reference planes of both waveguide ports were shifted to coincide with the metallic surfaces of the resonant sheets.

resonant behavior of multilayer metasurface filters. The combination of the equivalent circuit model, power-wave formulation, and transfer-matrix representation enables direct computation of the expected resonance frequencies and bandwidth variations prior to full-wave simulation. This integration ensures that the numerical analysis performed in this section is not a repetition of standard theory but a validation of the predictive capability of the developed model for both CSRR and Ω-type inclusions.

The final geometrical parameters of the filters were obtained directly from the analytical relations derived in Section 2, which link the resonance frequency f_0 to the equivalent inductance and capacitance through the outer radius r_{ext} and the slot spacing d (see Eq. (1)). Consequently, no numerical optimization procedure was required, as the analytical model accurately predicts the resonant behavior of each topology. Only a minor parametric verification of the interlayer separation l was conducted to confirm the absence of undesired mutual coupling between plates, with negligible computational effort. The design process was therefore driven by theoretical modeling rather than iterative numerical tuning.

The following analysis extends the study to the multilayer case, focusing on the two-layer configuration, which demonstrates the bandwidth enhancement predicted by the transfer-matrix model. The proposed model was validated through full-wave simulations using a WR340 waveguide configuration, as shown in Figure 15. An increase in the passband bandwidth is observed, in agreement with the theoretical predictions. However, a slight discrepancy in the transmission coefficient magnitude arises due to material losses included in the simulation, specifically the finite conductivity of aluminum, which leads to energy dissipation not considered in the ideal (lossless) model. These results highlight the importance of accounting for ohmic and radiation losses in practical analyses of metamaterial filters, particularly at frequencies where conductor properties significantly affect performance.

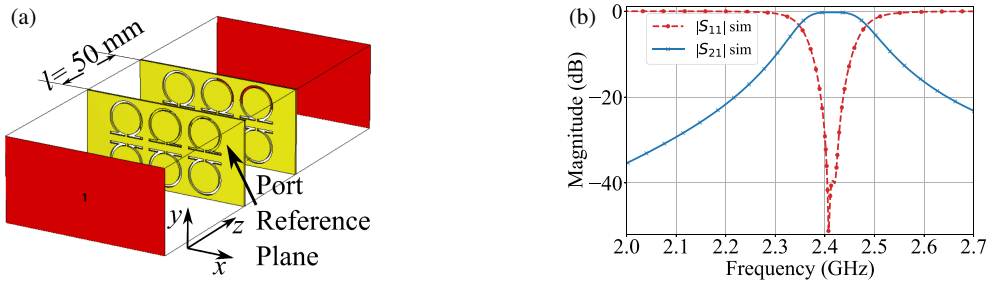

FIGURE 16. Simulation of a two-layer Ω-cell filter. (a) Three-dimensional model in a WR340 waveguide with an interlayer spacing l. (b) Simulated scattering parameters S_{11} and S_{21}. In this configuration, the reference planes of the input and output ports were aligned with the metallic surfaces containing the Ω arrays.

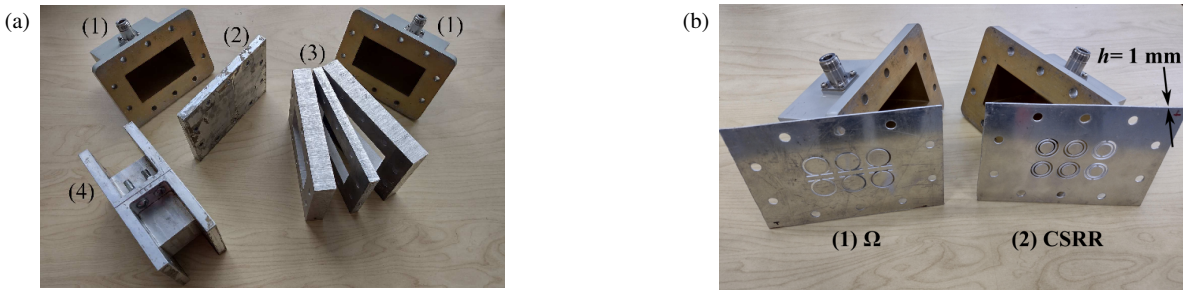

FIGURE 17. Laboratory elements for waveguide measurements. (a) Measurement accessories: (1) coaxial-to-waveguide adapters (340WCAN), (2) short-circuit plane, (3) aluminum spacers (two of 20 mm and one of 10 mm), and (4) reference line section of 57 mm. (b) Fabricated metallic sheets of thickness $h = 1$ mm: (1) Ω array and (2) CSRR array.

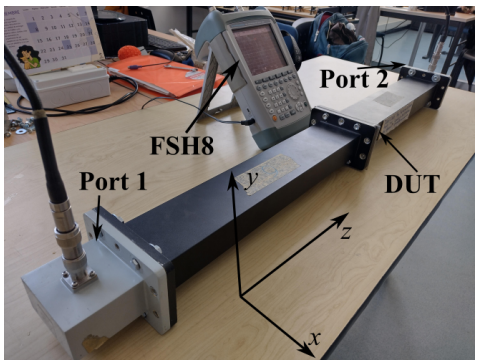

FIGURE 18. Experimental setup for the measurement of the CSRR and Ω-based filters in WR340 waveguide. The system includes the Rohde & Schwarz FSH8 vector network analyzer, coaxial-to-waveguide adapters, and WR340 extension sections.

Analogously to the CSRR case, a numerical simulation was performed to evaluate a filter composed of two layers of Ω-type cells. Figure 16(a) shows the three-dimensional model implemented in a WR340 waveguide, where the metallic sheets are separated by $l = 50$ mm to avoid undesired interlayer coupling. Aluminum was used as the conducting material to assess the impact of conductor losses on the filter response. The simulated scattering parameters in Figure 16(b) exhibit a bandpass behavior that agrees more closely with the theoretical model in Figure 14(a) than in the CSRR case. This improved agreement is attributed, on the one hand, to lower conduction losses for the Ω cells in the operating band and, on the other hand, to the broader bandwidth observed in simulation, which better matches the prediction of the transmission-matrix-based model. These results underscore the advantage of Ω-type structures for implementing wideband metamaterial filters with reduced sensitivity to conductor losses.

In all full-wave simulations, the reference planes of the waveguide ports were shifted to coincide exactly with the metallic surfaces containing the resonant arrays, as illustrated in Figures 15 and 16. This adjustment ensures that the S-parameters are computed directly at the physical boundaries of the filter, eliminating the contribution of the empty waveguide sections and providing a one-to-one correspondence with the experimental configuration. The same reference-plane alignment was applied to both input and output ports, enabling accurate comparison with the reference-plane aligned measurements.

All simulations were performed in the frequency domain using a finite-element-based full-wave solver. Waveguide ports and boundary conditions were configured to avoid unnecessary mesh refinement and to maintain numerical stability, ensuring accurate results with moderate computational cost. Each frequency sweep required less than one minute of computation on a workstation equipped with an AMD Ryzen 9 5900X processor (12 cores, 3.7 GHz), 8 GB of RAM, and a 512 GB NVMe solid-state drive.

The circuit- and full-wave simulations predict the expected passband widening when two mirror-symmetric sheets are combined. Further quantitative comparison with measured data and quality-factor analysis is presented in Section 4.

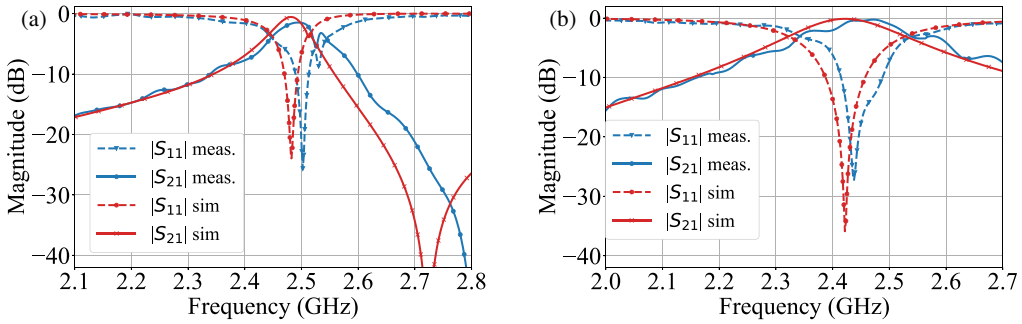

FIGURE 19. Measured and simulated S_{11} and S_{21} responses for a single mirror-symmetric layer: (a) CSRR array, (b) Ω-cell array. A good agreement is observed between simulation and measurement in both amplitude and resonance frequency. Small frequency shifts are consistent with the dimensional sensitivity discussed in Section 2, while minor ripples, present in both simulated and measured traces, originate from the intrinsic resonant behavior of the inclusions rather than from residual reflections at the transitions.

4. EXPERIMENTAL VALIDATION

For the experimental validation, mirror-symmetric arrays of CSRR and Ω cells were fabricated on AI1100 aluminum sheets (high-purity alloy) with a thickness of 1 mm. These metallic plates were designed to integrate with WR340 waveguide-to-coax adapters for direct characterization. Figure 17 shows the laboratory elements used in the measurements, including the adapters, short-circuit plane, precision spacers, and the fabricated metamaterial sheets for both resonator types. The metallic components were manufactured by high-precision waterjet cutting, a cold process capable of machining aluminum plates up to 300 mm thick with an accuracy of ± 0.1 mm, ensuring dimensional consistency and preventing thermal distortion of the resonant apertures.

The experimental setup is shown in Figure 18. Measurements were performed using a Rohde & Schwarz FSH8 vector network analyzer (VNA) in the 1.9 GHz–3 GHz range, together with WR340 waveguide extensions. A standard SOLT calibration was first applied at the coaxial ports using the FSH-Z28 calibration kit, which is the manufacturer-supplied calibration kit for the FSH8 VNA. Afterwards, a reference-plane alignment equivalent to a thru-reflect-line (TRL) adjustment, following the procedure described by Pozar [28], was carried out in the waveguide section to de-embed the adapters and the transition lengths. The "thru" corresponded to a direct WR340 connection, the "reflect" to a metallic short, and the "line" to a precision WR340 section of 57 mm. This combined SOLT+TRL workflow minimized fixture-dependent phase errors and improved measurement repeatability, yielding responses that closely matched the simulated behavior and confirming the accuracy of the multilayer model. It should be noted that this procedure does not replace a full TRL calibration executed within the VNA; rather, it provides an equivalent reference-plane correction in the waveguide domain, sufficient to de-embed the fixture lengths and enable meaningful comparison with the simulations.

Figure 19 shows the measured and simulated S_{11} and S_{21} responses for a single mirror-symmetric layer of each resonator type. To minimize reflections and suppress higher-order mode excitation, additional WR340 waveguide sections of different lengths were inserted, and the ports were positioned asymmetrically with respect to the DUT. This is a standard technique to break standing-wave periodicity. The measured curves show a good agreement with the simulations in both amplitude and resonance frequency. Small frequency shifts are attributed to the sensitivity of the resonant inclusions to dimensional tolerances, as discussed in Section 2 and summarized in Table 1. Likewise, minor ripples appear in both simulated and measured responses, indicating that they originate from the intrinsic behavior of the resonators rather than from residual reflections at the transitions. Overall, these observations confirm the consistency between the experimental and simulated responses and support the validity of the proposed analytical model.

After validating the single-layer structures, a two-layer mirror-symmetric configuration was fabricated to experimentally evaluate the bandwidth enhancement predicted by the circuit and transfer-matrix models. The metallic sheets were separated by a total distance of 50 mm (two 20 mm and one 10 mm aluminum spacers), ensuring minimal capacitive coupling between layers. Figure 20 compares the measured and simulated results, demonstrating a clear widening of the passband in both cases. The Ω-based filter exhibits a broader transmission band and the correspondingly lower insertion loss associated with its stronger interlayer coupling coefficients, consistent with the bandwidth-loss relationship of resonator-based filters.

Following the approach of Ortiz et al. [23], an *effective unloaded quality factor* (Q_u) was included to compare the loss behaviour of both multilayer filters under identical coupling conditions. It is important to emphasize that this Q_u is *not* the intrinsic quality factor of a single resonator as defined in classical narrow-band filter theory [29]; rather, it is a practical figure of merit obtained from the measured or simulated Q_L and insertion loss of the complete two-layer structure. This effective Q_u therefore characterizes the overall loss performance of each implementation and enables a consistent and physically meaningful comparison between the CSRR and Ω configurations. The extracted values reported in Table 2 quantify the relative dissipation and external coupling of both topologies and provide a consistent basis for interpreting the bandwidth-loss trade-offs exhibited by the multilayer implementations.

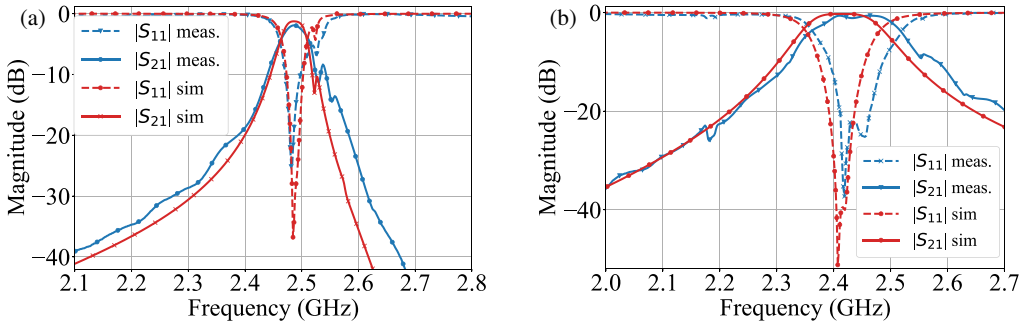

FIGURE 20. Measured and simulated S_{11} and S_{21} responses for two-layer mirror-symmetric filters: (a) CSRR-based configuration and (b) Ω-based configuration. A good agreement is observed between the simulated and measured responses, both in amplitude and resonant frequency. The results verify the expected bandwidth broadening produced by multilayer coupling. Minor deviations in frequency and amplitude are consistent with manufacturing tolerances and alignment sensitivity inherent to subwavelength resonant structures.

TABLE 2. Comparison among theoretical, simulated, and measured parameters for two-layer CSRR and Ω filters.

Topology	Method	f_0 [GHz]	BW [MHz]	FBW [%]	Q_L	IL [dB]	Q_u
CSRR	Model	2.47	98.9	4.00	25.0	–	–
CSRR	Simulation	2.49	45.9	1.81	55.3	1.26	410
CSRR	Measurement	2.48	51.5	2.07	48.15	1.92	243
Ω	Model	2.36	218.3	9.27	10.8	–	–
Ω	Simulation	2.41	136.5	5.65	17.7	0.27	578
Ω	Measurement	2.43	151.0	6.20	16.0	0.63	229

TABLE 3. Performance comparison of waveguide metamaterial bandpass filters.

Reference	Topology	f_0 (GHz)	FBW (%)	IL (dB)	Q_u
[23]	CSRR 1 — Layer	3.0	0.73	5.27	619.16
[10]	CSRR 3 — Layers	9.92	18.18	1	90.3
[24]	CL-SRR 3 — Layers	10.03	18.74	0.49	97.3
[9]	SRR 3 — Layers	10.01	5.69	0.38	350
[8]	CSRR+iris 4 — Layers	6.0	2	0.46	1850
This work	CSRR 2 Layers — 6 cells	2.48	2.07	1.92	243
This work	Ω 2 Layers — 6 cells	2.43	6.2	0.63	229

Note: Reported Q_u values reflect the definitions used in each reference. In this work, Q_u corresponds to an effective unloaded quality factor of the complete multilayer filter, not to the intrinsic resonator Q.

Table 3 summarizes representative CSRR-based waveguide filters reported in the literature, including single-layer designs [23], high-Q iris-coupled configurations [8], and complementary-loaded SRR (CL-SRR) structures [24]. The table also lists the present CSRR and Ω arrays composed of six unit cells and two metallic layers, allowing direct comparison in terms of fractional bandwidth, insertion loss, and Q_u. The proposed Ω filter achieves a fractional bandwidth of 5.6% with lower insertion loss (0.27 dB), representing a substantial improvement over the CSRR implementation while preserving compactness and manufacturability. These results confirm that the developed modeling and synthesis framework effectively predicts and tailors the bandwidth behavior of different resonator topologies within a unified multilayer approach.

5. CONCLUSIONS

This work has presented the design, modeling, and experimental validation of metamaterial-based waveguide filters using CSRR and Ω-type resonant inclusions. A unified analytical-numerical framework combining equivalent circuit models, surface polarizability extraction, and full-wave simulations was developed to predict and optimize the frequency response of multilayer configurations in WR340 waveguide.

The comparison between CSRR and Ω inclusions under mirror-symmetric configurations showed that both topologies exhibit dominant electric polarizability and negligible magnetic response, but with distinct behaviors in bandwidth and tolerance to interlayer spacing. CSRR cells provide narrowband

responses with high spectral selectivity, whereas Ω inclusions enable broader passbands and enhanced robustness to fabrication and alignment tolerances. The quantitative evaluation of the effective unloaded quality factor (Q_u) confirmed that both topologies exhibit comparable loss performance under identical coupling conditions, while the Ω configuration achieves lower simulated losses and improved bandwidth control due to stronger interlayer coupling.

Experimental measurements, performed with verified calibration and improved waveguide terminations, exhibited close agreement with simulations in terms of resonant frequency, bandwidth, and insertion loss, validating the predictive capability of the proposed transmission-matrix model.

These findings position Ω-based inclusions as an effective alternative for the realization of wideband waveguide filters, complementing the well-established use of CSRRs in narrowband selective applications. The presented methodology is scalable to multilayer configurations, providing a systematic route to bandwidth enhancement through controlled interlayer coupling. Moreover, it remains compatible with ongoing developments in high-Q CSRR-based waveguide filters [8], SIW implementations [6], and compact or wideband CSRR variants [7, 24].

In summary, the proposed framework bridges analytical modeling and experimental realization, offering a versatile and physically consistent approach for the synthesis of advanced metamaterial filters in the microwave and millimeter-wave regimes.

ACKNOWLEDGEMENT

This work was partly supported by Dirección de gestión de recursos para CTel — equipos salud (Convocatoria 844-2019 Ministerio de Ciencia, Tecnologıía e Innovación, Colombia), project code 130884467291.

REFERENCES

[1] Pendry, J. B., A. J. Holden, D. J. Robbins, and W. J. Stewart, "Magnetism from conductors and enhanced nonlinear phenomena," *IEEE Transactions on Microwave Theory and Techniques*, Vol. 47, No. 11, 2075–2084, 1999.

[2] Falcone, F., T. Lopetegi, M. A. G. Laso, J. D. Baena, J. Bonache, M. Beruete, R. Marqués, F. Martín, and M. Sorolla, "Babinet principle applied to the design of metasurfaces and metamaterials," *Physical Review Letters*, Vol. 93, No. 19, 197401, Nov. 2004.

[3] Bonache, J., I. Gil, J. Garcia-Garcia, and F. Martin, "Novel microstrip bandpass filters based on complementary split-ring resonators," *IEEE Transactions on Microwave Theory and Techniques*, Vol. 54, No. 1, 265–271, 2006.

[4] Marqués, R., J. Baena, J. Martel, F. Medina, F. Falcone, M. Sorolla, and F. Martín, "Novel small resonant electromagnetic particles for metamaterial and filter design," in *Proc. ICEAA*, Vol. 3, 439–442, Torino, Italy, 2003.

[5] Martel, J., R. Marques, F. Falcone, J. D. Baena, F. Medina, F. Martin, and M. Sorolla, "A new LC series element for compact bandpass filter design," *IEEE Microwave and Wireless Components Letters*, Vol. 14, No. 5, 210–212, 2004.

[6] Dong, Y. D., T. Yang, and T. Itoh, "Substrate integrated waveguide loaded by complementary split-ring resonators and its applications to miniaturized waveguide filters," *IEEE Transactions on Microwave Theory and Techniques*, Vol. 57, No. 9, 2211–2223, 2009.

[7] Bahrami, H., M. Hakkak, and A. Pirhadi, "Using complementary split ring resonators (CSRR) to design bandpass waveguide filters," in *2007 Asia-Pacific Microwave Conference*, 1–4, Bangkok, Thailand, 2007.

[8] Aparicio, A. O., J. H. Jiménez, F. D. Q. Pereira, and A. A. Melcón, "Design of rectangular waveguide bandpass filters with transmission zeros using high-Q_u complementary split-ring resonators with irises," *IEEE Transactions on Microwave Theory and Techniques*, Vol. 73, No. 2, 1073–1084, 2025.

[9] ——, "Design of evanescent-mode rectangular waveguide inline bandpass filters with transmission zeros using split ring resonators," *IEEE Transactions on Microwave Theory and Techniques*, Vol. 72, No. 7, 4246–4257, 2024.

[10] Bage, A. and S. Das, "Stopband performance improvement of CSRR-loaded waveguide bandpass filters using asymmetric slot structures," *IEEE Microwave and Wireless Components Letters*, Vol. 27, No. 8, 697–699, 2017.

[11] Díaz, I. E., J. D. Baena, and C. A. Suárez, "Waveguide filters based on metasurfaces made of subwavelength slot resonators," in *2022 Sixteenth International Congress on Artificial Materials for Novel Wave Phenomena (Metamaterials)*, 40–42, Siena, Italy, 2022.

[12] Marqués, R., F. Medina, and R. Rafii-El-Idrissi, "Role of bianisotropy in negative permeability and left-handed metamaterials," *Physical Review B*, Vol. 65, No. 14, 144440, 2002.

[13] Baena, J. D., J. Bonache, F. Martin, R. M. Sillero, F. Falcone, T. Lopetegi, M. A. G. Laso, J. Garcia-Garcia, I. Gil, M. F. Portillo, and M. Sorolla, "Equivalent-circuit models for split-ring resonators and complementary split-ring resonators coupled to planar transmission lines," *IEEE Transactions on Microwave Theory and Techniques*, Vol. 53, No. 4, 1451–1461, 2005.

[14] Pulido-Mancera, L. M. and J. D. Baena, "Equivalent circuit model for thick split ring resonators and thick spiral resonators," in *2014 IEEE Antennas and Propagation Society International Symposium (APSURSI)*, 2084–2085, Memphis, TN, USA, 2014.

[15] Marqués, R., F. Martín, and M. Sorolla, *Metamaterials with Negative Parameters: Theory, Design, and Microwave Applications*, John Wiley & Sons, 2008.

[16] Bahl, I. J. and P. Bhartia, *Microwave Solid State Circuit Design*, John Wiley & Sons, 2003.

[17] Díaz-Pardo, I., C. A. Suárez-Fajardo, G. Puerto-Leguizamón, and T. Zona-Ortiz, "Band-pass filters using OSRR cells," *Revista Facultad de Ingeniería Universidad de Antioquia*, Vol. 74, 60–69, 2015.

[18] Marques, R., F. Mesa, J. Martel, and F. Medina, "Comparative analysis of edge- and broadside-coupled split ring resonators for metamaterial design-theory and experiments," *IEEE Transactions on Antennas and Propagation*, Vol. 51, No. 10, 2572–2581, 2003.

[19] Pulido-Mancera, L. M., J. D. Baena, and J. L. A. Quijano, "Thickness effects on the resonance of metasurfaces made of SRRs and C-SRRs," in *2013 IEEE Antennas and Propagation Society International Symposium (APSURSI)*, 314–315, Orlando, FL, USA, 2013.

[20] Baena, J. D. and L. M. Pulido-Mancera, "Controlling the cross-polarization effects of metasurfaces from the lowest to the highest possible value," in *2015 9th International Congress on Advanced Electromagnetic Materials in Microwaves and Optics*

(METAMATERIALS), 367–369, Oxford, UK, 2015.

[21] Tretyakov, S., *Analytical Modeling in Applied Electromagnetics*, Artech House, 2003.

[22] Diaz, I., C. A. S. Fajardo, J. D. B. Doello, and H. Guarnizo, "Sub-wavelength resonator for the design of a waveguide-fed metasurface antenna," *Progress In Electromagnetics Research C*, Vol. 156, 113–120, 2025.

[23] Ortiz, N., J. D. Baena, M. Beruete, F. Falcone, M. A. G. Laso, T. Lopetegi, R. Marqués, F. Martín, J. García-García, and M. Sorolla, "Complementary split-ring resonator for compact waveguide filter design," *Microwave and Optical Technology Letters*, Vol. 46, No. 1, 88–92, 2005.

[24] Bage, A. and S. Das, "A compact, wideband waveguide band-pass filter using complementary loaded split ring resonators," *Progress In Electromagnetics Research C*, Vol. 64, 51–59, 2016.

[25] Smith, D. R., M. Sazegar, and I. Yoo, "Equivalence of polarizability and circuit models for waveguide-fed metamaterial elements," *IEEE Transactions on Antennas and Propagation*, Vol. 73, No. 1, 7–21, 2025.

[26] Pfeiffer, C. and A. Grbic, "Metamaterial Huygens' surfaces: Tailoring wave fronts with reflectionless sheets," *Physical Review Letters*, Vol. 110, No. 19, 197401, May 2013.

[27] Gonzalez, G., *Microwave Transistor Amplifiers: Analysis and Design*, Prentice Hall, New Jersey, 1997.

[28] Pozar, D. M., *Microwave Engineering: Theory and Techniques*, 4th ed., John Wiley & Sons, 2012.

[29] Swanson, D. G., "Narrow-band microwave filter design," *IEEE Microwave Magazine*, Vol. 8, No. 5, 105–114, 2007.